Computers and Electronics in Agriculture 207 (2023) 107749

Contents lists available at ScienceDirect

Computers and Electronics in Agriculture

journal homepage: www.elsevier.com/locate/compag

3D laser imaging for measuring volumetric shrinkage of horticultural products during drying process

Kaveh Mollazade[a,b,*], Joschka van der Lucht[b], Sven Jörissen[b], Andreas Nüchter[b]

[a] Department of Biosystems Engineering, Faculty of Agriculture, University of Kurdistan, Sanandaj, Iran
[b] Informatics XVII: Robotics, Julius-Maximilians-University Würzburg, Am Hubland, Würzburg 97074, Germany

ARTICLE INFO

Keywords:
Image processing
Point clouds
3D laser imaging
Triangulation
Volume measurement
Volumetric shrinkage

ABSTRACT

The standard method of shrinkage measurement consists of immersion of the product in a fluid in order to calculate the volume changes before and after drying. It is destructive and time-consuming and also is not a practical method to be used in online drying monitoring systems. To date, it has been tried for measuring shrinkage based on passive stereo vision. But no report has been provided so far on the accuracy of this technique and its comparison with conventional method of measuring volumetric shrinkage. On the other hand, because of the small size of dried foodstuff products, it does not seem that the stereo vision to be able to extract high detail point clouds from the surface of objects. Therefore, this research was conducted in order to study the potential use of 3D laser scanning for measurement of the volumetric shrinkage of some horticultural products during drying process. To this end, a calibrated 3D laser imaging system was applied in order to precisely scan the surface of some small size horticultural products (including plum, fig, date, and button mushroom), which take non-symmetric form during the drying process. 2D image of samples was also taken to predict the volumetric shrinkage by various texture analysis methods. Drying was carried out by a convective dryer. The results indicated a significant superiority of 3D laser imaging compared to 2D imaging. The value of correlation coefficient and mean absolute percentage error of multilayer perceptron artificial neural networks models created based on selected spatial features of point clouds in predicting volumetric shrinkage for plum, fig, date, and mushroom was obtained 0.90 and 19.48, 0.95 and 14.25, 0.78 and 23.54, and 0.87 and 9.47, respectively.

1. Introduction

Drying is one of the most significant post-harvest processes in which decreasing moisture content and water activity to reach the hygroscopic equilibrium not only prevents food materials from microbial attack and decaying but also increases their retention time (Mujumdar, 2004). Because of enzymatic/non-enzymatic browning reactions and loss of water, drying is accompanying with a number of physicochemical changes in the majority of foodstuffs like changes in pigments, loss/reduction of nutritional elements, tissue hardening, and changes in texture and shape (Nindo et al., 2003). During drying, fruits/veggies lose moisture gradually from the center to the external surfaces. This event collapses cellular membranes due to an unbalance pressure between internal and external parts of the material and as a consequent result the viscoelastic matrix of matter is drawn into the void spaces caused by evaporation and finally shrinkage, which is a reduction in the shape and size of food tissues, occurs (Bonazzi and Dumoulin, 2011; Aprajeeta et al., 2015).

It has been proven that moisture content and shrinkage are linearly correlated so that shrinkage increases by decreasing moisture content for a wide variety of horticultural products (Dehghannya et al., 2016). On the other hand, shrinkage affects the thermo-physical properties of food matter, heat and mass transfer phenomena, and the effective humidity diffusion coefficient. It also reduces dehydration ability and causes surface cracking of the product that adversely affect product marketing (Mayor and Sereno, 2004). Different horticultural products have different shrink-ability and its severity highly depends on the drying method. For example, shrinkage in the hot air drying and microwave drying methods is stronger than freeze drying because of an increase in the rate of cellular deformation due to the raised temperature following an Arrhenius-type behavior (Yadollahinia and Jahangiri, 2009).

Microstructure of fruits/veggies is highly affected by drying conditions and irreversible tissue changes can happen rapidly, which may

* Corresponding author at: Department of Biosystems Engineering, Faculty of Agriculture, University of Kurdistan, Sanandaj, Iran.
E-mail address: k.mollazade@uok.ac.ir (K. Mollazade).

https://doi.org/10.1016/j.compag.2023.107749
Received 19 March 2022; Received in revised form 29 January 2023; Accepted 28 February 2023

result in the degradation of product quality. Therefore, it is necessary to monitor and control the physico-mechanical changes of the product's texture, like shrinkage, during drying process to maintain quality (Lewicki and Jakubczyk, 2004). The common methods to measure the shrinkage include direct measurement using micrometer or measuring volume changes by fluid displacement (liquid pycnometry) method. Whereas these methods are considered as reference for shrinkage measurement, as the main drawbacks, they are highly time-consuming, destructive, and cannot be applied in practice for real-time/online measurements. Hence, various kinds of research have been conducted during the last two decades to find a reliable alternative approach to measure shrinkage in the non-contact manner. Most of the works that have been conducted involves the use of shape and textural features of 2D images to predict shrinkage (Raponi et al., 2017). Despite relatively appropriate results (high correlation coefficient and low error rate) of measuring shrinkage in drying of thin layer specimens (Behroozi Khazaei et al., 2013; Jafari and Bakhshipour, 2014), it cannot be employed as a general method with acceptable accuracy, especially if the thickness of the specimens increases, the thickness is not uniform across the sample, or the shape of product is irregular and complex. Thus, it is required to apply 3D shape contours in order to measure volume changes. 2D X-ray Computerized Tomography (CT) cross-sections have been employed to measure shrinkage by reconstructing 3D shape of dried samples (Danvind and Synnergren, 2001; Li et al., 2014). While the CT scanning is accurate, some disadvantages, such as cost of equipment, long data acquisition time, and complexity of image processing algorithms due to high volume of information obtained, make it inappropriate in practice to be used in dryers. Madiouli et al. (2011) introduced a novel non-intrusive technique based on 3D Digital Image Correlation method (3D-DIC) or stereo-correlation to determine the apparent volume of banana samples in a convective dryer. The main disadvantage of this study is that the results obtained by the 3D stereo vision method have not been validated by the reference volume measurement method. On the other hand, it is not possible to obtain high resolution point clouds data by the stereo vision when the size of dried products is small. In return, 3D laser imaging with simple setups at highly low cost is extremely reliable at detecting objects of sufficient size. Therefore, it seems 3D laser imaging can provide more reliable results compared to the stereo vision in measuring volumetric shrinkage of horticultural products, when their shape becomes thin, irregular, and non-symmetric during drying. 3D laser imaging, which is also known as triangulation-based scanning, is an active imaging method that uses a laser stripe to scan the scene. A camera is used to record the location of the laser line. Depending on how far away the laser strikes an object, the laser line appears at different places in the camera's field of view. Having the distance between the image sensor of camera and the laser emitter, the angle of the camera corner, and the angle of laser emitter corner, the height information can be calculated by triangulation formula (Mollazade et al., 2021). Heating-induced volume shrinkage of meat cuboids has been estimated using the terrestrial 3D laser scanning technology (Vaskoska et al., 2020). While the obtained results were promising, due to the relatively long imaging time and the need for completely reconstruction of the 3D shape of samples for volume measurement, the proposed technique is not effective in practice for use in real-time applications. Accordingly, this research was conducted in order to develop a non-contact approach based on 3D laser imaging to measure volumetric shrinkage of some horticultural products during drying process in real-time. The aim of the study was achieved through the following objectives:

- Monitoring of volumetric shrinkage changes of small size horticultural products in hot air drying process
- Geometric validation of the 3D laser imaging system for scanning of small size fruit -shape artificial objects with predefined volumes
- Introducing some spatial features in processing of point clouds of laser scans
- Evaluating the performance of the 3D laser imaging system in measuring volumetric shrinkage of dried horticultural products in comparison with the 2D imaging and conventional fluid displacement method

2. Materials and methods

2.1. Sample preparation

Fresh samples including plum, fig, date, and button mushroom were purchased from the local markets in Würzburg, Germany (40 samples each). The oven drying method was applied in order to determine the moisture content of fresh samples (AACC, 1986). Eight samples from each fruit and mushroom were randomly selected. After weighing (W_1), they were kept at the drying condition (75 °C) until reaching a constant weight (W_2). The moisture content (MC) of samples (wet basis) was then calculated as following:

$$MC(\%, w.b.) = \left(\frac{W_1 - W_2}{W_1}\right) \times 100 \tag{1}$$

After drying, it was specified that the samples have initial MC of 49.81, 67.71, 20.03, and 91.63 % w.b. for plum, fig, date, and mushroom, respectively. The rest of samples were stored in plastic bags at refrigeration condition (4 °C) until the experiments were carried out. Samples were stored in refrigerator for less than 15 h. Since the samples were kept in plastic bags, it is expected that they retained their moisture content and no decreasing in the initial moisture content of samples has been occurred.

2.2. Data collection

Samples were removed from the cold storage two hours prior experiments to let them reach room temperature. Samples were first taken for the mass determination. The apparent volume (V_s (cm^3)) of samples was then calculated using the fluid displacement method by a pycnometer as follows (Yan et al., 2008):

$$V_s = \frac{(W_{pf} - W_p) - (W_{pfs} - W_{ps})}{\rho_f} \tag{2}$$

where, W_p, W_{pf}, W_{ps}, W_{pfs}, and ρ_f are mass of pycnometer (g), mass of pycnometer containing fluid (g), mass of pycnometer containing sample (g), mass of pycnometer containing fluid and sample (g), and apparent density of fluid (g/cm^3), respectively.

After drying the surface of the samples with a cloth, 2D imaging and 3D laser imaging were taken place. The samples were then placed in a dryer. During drying, 5 samples were taken out of the dryer every 2 h (there was 7 samples at the end of drying). 2D imaging and 3D laser imaging were performed from these samples and after measuring their mass, the fluid displacement method and Equation (2) were used to measure their volume. Finally, the volumetric shrinkage (S) was calculated using the following equation (Yan et al., 2008):

$$S = \left(1 - \frac{V_t}{V_0}\right) \times 100 \tag{3}$$

where, V_0 and V_t are the apparent volume of samples at fresh stage and drying stage *t*, respectively.

A home-scale convective hot-air dryer was applied to dry the samples (VITA5 Nobel PRO, Netherland). The hot air heated by the electric heating tube was blown into the drying chamber by a centrifugal fan. An axial flow fan, located in the middle of the end side of the drying chamber, provided uniform circulation and distribution of air flow in the drying chamber (airflow rate: 1.3 to 1.5 m/s.). Approximately an hour before the drying process began the dryer was turned on to the temperature inside the dryer to be stable. Then, the samples were placed on the central tray of the dryer in such a way that there was a suitable

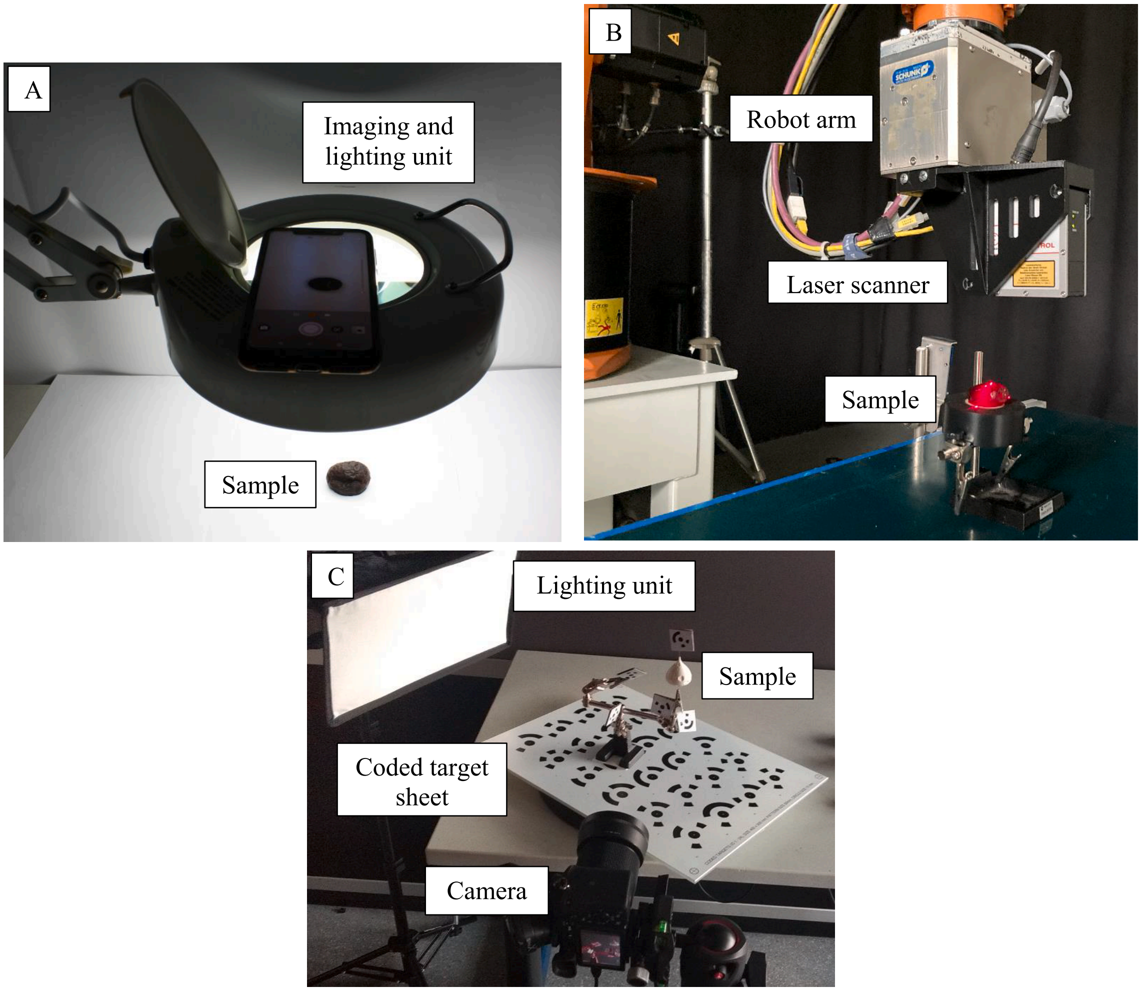

Fig. 1. Imaging setups: A) 2D imaging, B) 3D laser imaging, and C) Photogrammetry.

distance between the samples for air circulation. The mass of the samples was measured and recorded with a digital scale with an accuracy of 0.01 g (Brifit, model KA26, China) before drying and once every hour during drying, to inform the process of moisture reduction and to draw the drying curve. The samples were dried for 12 h. Drying temperature was determined based on literature review, it was 60° C (Sacilik et al., 2006), 70° C (Sarvestani et al., 2014), 70° C (Al-Awaadh et al., 2015), and 60° C (Li et al., 2021) for plum, fig, date, and mushroom, respectively.

Since the method presented in the current research for predicting volumetric shrinkage of dry fruits based on the spatial features of point clouds (section 2.3.2) is completely novel and there was no similar research to provide a comparison, it was done with result of predicting volumetric shrinkage of dry fruits based on the texture analysis of 2D images (section 2.3.1), which is the only introduced non-contact shrinkage measurement method. The setup shown in Fig. 1-A was used to acquire 2D images. The images were acquired by a mobile phone camera (Motorola one, 13 MP, f /2.0, 1/ 3.1 ", 1.12 µm, PDAF, China) and at a height of 35 cm from the surface of the samples. Settings of camera went out the automatic mode in order to acquire images with the same conditions. A 22-watt fluorescent lamp was used as the light source. Since the lamp was circular and created daylight, the scene was uniformly illuminated so that no shadow was created around the samples. For the sample segmentation to be made easier, the background was considered white for plums, figs, and dates, and the background was considered black for button mushrooms.

3D point clouds of samples were acquired using a calibrated high-speed laser profile scanner (Micro-Epsilon scanControl 2900–25, Micro-Epsilon Messtechnik GmbH & Co. KG, Germany). Micro-Epsilon scanControl 2900–25 is a high precision laser scanner, which has been designed for use in industrial and laboratory applications. Point clouds generated by this scanner is highly accurate so that minimum number of scattered points is assured by the manufacturer. Equipped with a 658 nm low power Class 2 M semiconductor linear laser and a CMOS image sensor, the laser scanner was mounted on the flange of a 6-axis KUKA KR16 robot (±0.05 mm repeatability) to scan the samples from the top (Fig. 1-B). The Micro-Epsilon scanner measures a scan line at a time [z-axis (height) resolution: ±2 µm, z-axis measuring range: 25 mm (starting at 53.5 mm and ending at 78.5 mm), x-axis resolution: 1280 points/profile, and x-axis measuring range (the scanning width per line): 23.4 mm to 29.1 mm]. The top surface of samples was scanned by moving the robot arm in the horizontal direction at linear speed of 7.2 mm/s. The height information of the reflected laser light, which is collected by the camera, is calculated by the triangulation method. The same setup was used for earlier work in Mollazade et al., 2021. The scanner geometric calibration was carried out by KUKAs internal *XYZ – 4 Point* and *ABC – 2 Point* methods to determine position and orientation of the Tool Center Point (TCP) with respect to the robot's base coordinate system. Since the scanning width was 23.4–29.1 mm, the KUKA robot was programmed to scan the surface of samples in one plane over them with two consecutive sweeps. Therefore, there was sufficient overlap among two consecutive sweeps in order to ensure successive scanning of samples with various heights. After acquiring the point clouds of each sample, the data were stored in the.*xyz* format for further analysis.

Photogrammetry imaging method was used to geometrically validate the laser imaging system in scanning samples related to horticultural products. First, it was necessary to verify the function accuracy of the photogrammetry method. Therefore, the accuracy of the photogrammetry method in measuring the volume of objects was compared with the standard method of fluid displacement. For this purpose, the main, middle and sub-diameters of samples of plum, fig, date, and button mushroom with small and large sizes, were measured by a caliper. The criteria considered to define the size of the products was based on the literature review (Jahromi et al., 2008; Caglarirmak, 2011; Ionica et al., 2013; Ersoy et al., 2017). Then, the three-dimensional shape of these products was modeled in SOLIDWORKS® ver. 26 (Dassault Systèmes, Vélizy-Villacoublay, France) software. Finally, the models were printed with white filament by a 3D printer (Ultimaker S3, Ultimaker Co., Netherlands). The volume of printed samples was measured by the fluid displacement method (Section 2.2). The images of these samples were then taken by a photogrammetry imaging system, as follows.

As Fig. 1-C shows, the artificial (printed) samples were mounted on a stand using a small needle. Around this, some small coded targets were placed as unique identifiable features for the image reconstruction. A DinA4 float glass plate was placed under the stand, which was also printed with coded targets. The targets on the glass plate have a defined size and a fixed defined distance from each other. The distances between the center points of the markers on the glass plates are accurate to 0.100 mm. Thus, the plate serves on the one hand as a unique feature in the reconstruction and, on the other hand, can also be used as a scale bar to determine the scaling of the object. The entire assembly was on a turntable and can therefore be rotated around the center of the object without changing the assembly or the position between the markers and the object. Two flashes were used to guarantee perfect illumination and to adjust the exposure to the object. The employed camera was a Sony A6300 with a 30 mm lens. The image resolution was 6000 × 4000 pixel. The images were taken from three different angles. Once from eye level with the object and 45°each above and below it. For each angle, the object was rotated around its own axis and a photo was taken approximately every 5–10°. In addition, a photo was recorded from the vertical from above. Thus, the surface of the object was systematically recorded from all viewing angles with sufficient overlap of the individual images.

The 3D reconstruction was done using Agisoft Metashape ver. 1.8.1 software (Agisoft LLC, St. Petersburg, Russia). The accuracy achieved by photogrammetry using Agisoft on similar objects has already been studied by Schöning and Heidemann, 2015. The mean value of the deviation from the ground truth data was 4.52 mm. Since these investigations are based on a data set with a significantly lower resolution and a lower number of images, it can be assumed that results of the current study show an even higher precision. The workflow in Metashape is typical for a photogrammetric reconstruction and can be divided into two steps. The first step is the so-called alignment, in the second step the surfaces are reconstructed, meshes are generated and textures are applied. In the first step, feature points are searched for in the images and matched across images. Likewise, the camera positions for each image are determined and the intrinsic and extrinsic parameters of the camera are estimated. According to Agisoft, these steps are based on the work of Hirschmuller, 2007. In the second step, a 3D object is reconstructed from the previously determined correlations and a mesh is generated (Hiep et al., 2009; Poliarnyi, 2021). Then, this mesh is overlaid with the textures of the original images.

After meshing, the volume of samples were calculated. The measurement accuracy of the photogrammetric system was determined by calculating the amount of error between the volume measured by the photogrammetry method and the volume measured by the fluid displacement method. Next, point clouds were acquired from the printed samples by the laser imaging system (exactly similar to what was done for real samples). Then, the two point clouds, the laser scanning and the photogrammetry, were registered against each other and the point-to-point distance was calculated. Finally, the matching error rate between the obtained points was used as an evaluation criterion for the geometric validation of the laser scanning system.

2.3. *Feature extraction and modeling*

2.3.1. *2D imaging*

First, the 2D images were pre-processed (converted to the grayscale) to segment the sample from the background by the Otsu thresholding method. After segmentation, the closing and opening operators (using a disk shape structural element, radius = 5 pixels) were used to remove the imperfection areas in the background. In order to increase the size of the database, 10 areas with a size of 100 × 100 pixels were extracted from the bounding box image of each sample. These areas were randomly selected so that at least 95% of the pixels in them belong to the sample. Then, images related to these areas were saved on the computer. Statistical based methods were used to extract the textural features of preprocessed images (Mollazade and Arefi, 2017). Using this method, the sample size was increased to 320, which is in an acceptable amount for modeling. The features extracted from the first order statistics of image histogram (FOSH) and local binary pattern (LBP) were average, standard deviation, measure of smoothness, skewness (3rd moment), measure of uniformity (energy), entropy, kurtosis (4th moment), and coefficient of variation. Grey level co-occurrence matrix (GLCM) and grey level run length matrix (GLRLM) were calculated for each image in directions 0, 45, 90, and 135°. Ten features were extracted from each GLCM including: contrast, correlation, energy, homogeneity, entropy, maximum probability, dissimilarity, cluster shade, cluster prominence, and variance. The extracted features form the GLRLM were: short run emphasis, long run emphasis, gray-level non-uniformity, run length non-uniformity, run percentage, low gray-level run emphasis, high gray-level run emphasis, short run low gray-level emphasis, short run high gray-level emphasis, long run low gray-level emphasis, and long run high gray-level emphasis. The average of extracted features in all directions was determined to obtain the final GLCM and GLRLM features vector.

Multilayer perceptron artificial neural networks (MLP) were used to create volumetric shrinkage predictor models. Input of the models was the features extracted from the texture of the images and the output of the models was the actual volumetric shrinkage values of the samples obtained by the fluid displacement method. Since the scatter and scale of the input data varied, the data became normalized between zero and one. In order to prevent over-fitting, after data randomization, the data set was divided into three parts: training (including 65% of data), cross-validation (including 15% of data), and testing (including the rest of data). Levenberg-Marquardt algorithm was used for learning the models with a learning rate of 0.1. Transfer function of middle and end layers were selected as tangent sigmoid and linear, respectively. Since the performance of artificial neural networks is strongly influenced by its architecture, trial and error method was used to find the most suitable architecture. Accordingly, the most optimal performance of the models was achieved when the network architecture consists of a hidden layer with 4 neurons. Performance evaluation of models was performed using correlation coefficient (R), root mean square error (RMSE), and mean absolute percentage error (MAPE) (Mollazade and Arefi, 2017):

$$R = \frac{N\sum_{i=1}^{N} y_i\widehat{y}_i - \left(\sum_{i=1}^{N} y_i\right)\left(\sum_{i=1}^{N}\widehat{y}_i\right)}{\sqrt{\left(N\sum_{i=1}^{N} y_i^2 - \left(\sum_{i=1}^{N} y_i\right)^2\right)\left(N\sum_{i=1}^{N}\widehat{y}_i^2 - \left(\sum_{i=1}^{N}\widehat{y}_i\right)^2\right)}} \tag{4}$$

$$RMSE = \sqrt{\frac{\sum_{i=1}^{N}\left(\widehat{y}_i - y_i\right)^2}{N}} \tag{5}$$

$$MAPE = \frac{\sum_{i=1}^{N}\left|\frac{\widehat{y_i - y_i}}{y_i}\right|}{N} \times 100 \tag{6}$$

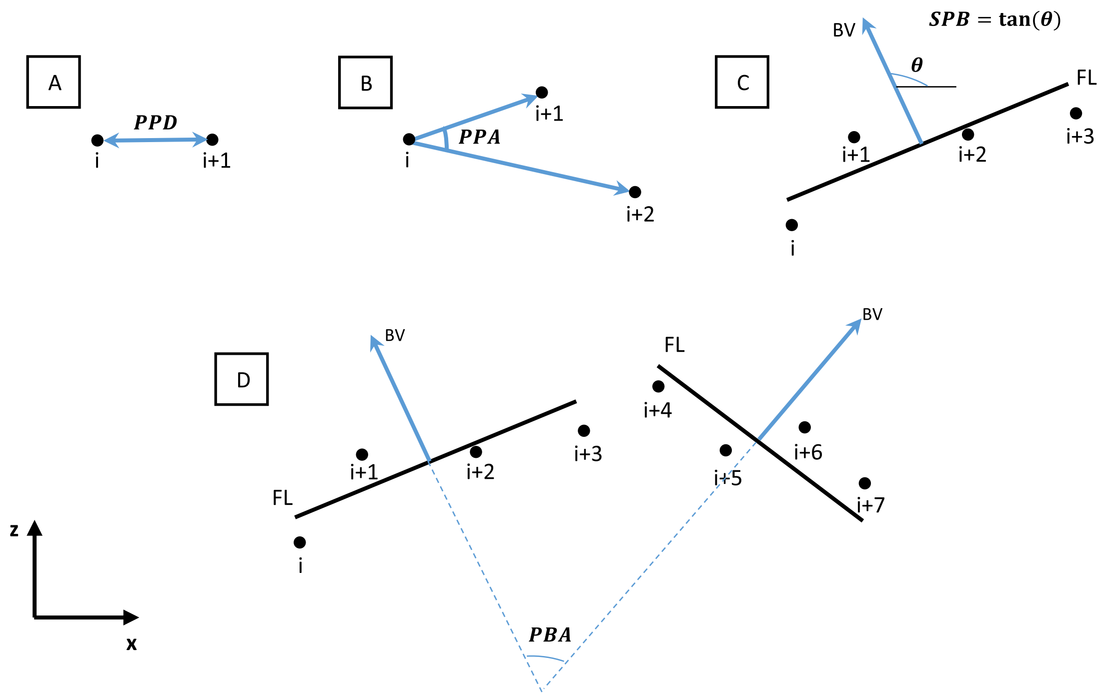

Fig. 2. Extracted spatial features from point clouds of each scan line: A) Point to point distance (PPD), B) Point to point vectors' angle (PPA), C) Slope of the perpendicular bisector vector (SPB), and D) Perpendicular bisector vectors' angle (PBA). BV and FL stand for bisector vector and fitting line, respectively. × and z are the scan line and height directions, respectively.

where, y_i, $\widehat{y}_i$, and N are target (actual) value, model predicted value, and total number of samples, respectively. The results were reported based on 20 replications in model training as mean ± standard deviation.

2.3.2. 3D laser imaging

Using the 3D laser imaging setup it was impossible to scan the entire body of samples due to the limitation exists for the full bending of the robot arm. Therefore, the point clouds were not available in 360-degree and it was impossible to directly calculate the sample volume from the point clouds. Of course, calculating volume based on point clouds is a complex and time-consuming process on the one hand, and requires strong processing hardware, on the other hand. Since the aim of this study was to provide a solution based on 3D laser imaging to measure the volumetric shrinkage of horticultural products in real time, it was predicted indirectly by extracting some spatial features from point clouds. From the obtained point clouds, four features were extracted as follows (Fig. 2):

Point to point distance (PPD)

This feature is actually the magnitude of the vector between two consecutive points in each scan line and is calculated as follows:

$$PPD = \sqrt{(x_{i+1} - x_i)^2 + (y_{i+1} - y_i)^2 + (z_{i+1} - z_i)^2} \tag{7}$$

where, x_i and x_{i+1}, y_i and y_{i+1},and z_i and z_{i+1} are the coordinates of two adjacent points in × (scan line), y (scanner moving), and z (height) directions, respectively. In each scan line, the y coordinates of points were the same. Therefore, $(y_{i+1} - y_i) = 0$.

Point to point vectors' angle (PPA)

This feature specifies the angle between the vector created by one point and the next point and the vector created by the same point and the next two points, on each scan line, in radians:

$$PPA = \arccos\left(\frac{PPD_{i,i+1}{}^2 + PPD_{i,i+2}{}^2 - PPD_{i+1,i+2}{}^2}{2(PPD_{i,i+1} \times PPD_{i,i+2})}\right) \tag{8}$$

where, $PPD_{i,i+1}$, $PPD_{i,i+2}$, and $PPD_{i+1,i+2}$ are the point to point distance between points i and $i+1$, i and $i+2$, and $i+1$ and $i+2$, respectively.

Slope of the perpendicular bisector vector (SPB)

To calculate this feature, the fitted linear function is calculated on 4 consecutive points in the scan line. Then, the slope of the perpendicular bisector vector of the fitted liner function is obtained by the following equation:

$$SPB = \frac{-1}{m} \tag{9}$$

where, m is the slope of the fitted linear function.

Perpendicular bisector vectors' angle (PBA)

This feature shows the angle between two consecutive perpendicular bisector vectors on the scan line in radians:

$$PBA = \arctan\left|\frac{SPB_i - SPB_{i+1}}{1 + (SPB_i \times SPB_{i+1})}\right| \tag{10}$$

where, SPB_i and SPB_{i+1} are the slope of consecutive perpendicular bisector vectors i and $i+1$, respectively.

The above mentioned features were extracted from the point clouds for each scan line. Then, the average values obtained for each feature were considered as the features extracted from each scan line. Therefore, the vector length of each of the extracted features was equal to the number of scan lines for each sample. In order to increase the size of the database, after randomization, the features matrix of each sample was divided into 10 sections in the same size. Using this approach, not only the effect of probable existing scattered points on the measurements was reduced but also the sample size for modeling was increased to 320. Finally, descriptive statistics including mean, standard deviation, kurtosis, and skewness were extracted from the absolute value of the matrix of features related to each section. MLP was used to create volumetric shrinkage predictor models. Input of the models was descriptive statistics extracted from the features obtained from the point clouds and output of the models was the actual volumetric shrinkage values of the samples obtained by the fluid displacement method. The creation and evaluation of MLP-based models were the same as in Section 2.5.1 that

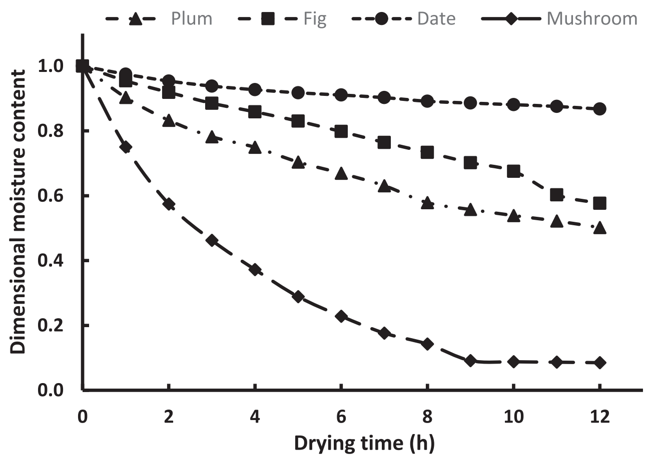

Fig. 3. Variation of moisture content of samples with drying time.

were described for modeling based on features extracted from the 2D images.

2.4. Software tools

The ANOVAs (one-way) and subsequent post-hoc Tukey's honest significance difference (HSD) tests were performed in Minitab® 16.2.2 (State College, PA, USA) in order to compare mean values of the volumetric shrinkage of samples at different drying times. A value of p less than 0.05 was considered as statistically significant. The KUKA KR C2 robot control with the KUKA Systems Software V5 (KUKA AG) along with an in-house built software tool (based on C++, Qt, and the MicroEpsilon scanControl SDK 0.2.0 for Linux) were employed in order to control of the robot and to acquire point cloud data. Photogrammetry images were processed in Agisoft Metashape ver. 1.8.1 software (Agisoft LLC, St. Petersburg, Russia). The 3D point clouds were visualized and matched in the open-source software CloudCompare 2.10.2 (Girardeau-Montaut, 2015). Processing of 2D images and feature extraction from 3D point cloud data were carried out in MATLAB® ver. R2015b (The MathWorks, Inc., Natick, Massachusetts, USA). The *LightScatter* toolbox in MATLAB was applied in order to extract the texture features from the 2D images and to generate the artificial neural networks' prediction models from the extracted features of 2D images and 3D point clouds (Mollazade and Arefi, 2017). MS Excel ver. 2013 (The Microsoft Inc., Redmond, Washington, USA) and MATLAB® ver. R2015b were used for plotting graphs.

3. Results and discussion

3.1. Drying characteristics of samples

Fig. 3 shows the changes in moisture content of different sample types during the drying process. The rate of moisture reduction in button mushrooms was higher than plums, figs and dates. The reason is that the initial moisture content of button mushrooms (91.63% w.b.) is higher compared to other products. In addition, at the beginning of the drying process, the moisture reduction is due to the evaporation of the surface moisture of the product. Over time, the surface moisture evaporates and the internal moisture of the product is transferred to the surface and evaporates. Since the button mushroom has no skin, the internal moisture of the product that has been transferred to the surface is exposed to hot air flow and evaporates immediately. However, if the skin of the sample is thicker or the pores of the skin are more capillary, the internal moisture evaporates at a lower speed compared to the surface moisture. In such cases, as the drying time increases, more moisture from the inner parts of the sample accumulates under the skin. This issue increases the pressure under the skin of the sample. If the pressure is greater than the tensile strength of the fruit skin, the skin cracks and as a result, the moisture accumulated under the fruit skin is transferred to its surface and the drying rate increases. Since the skin of the plum is thinner than the fig, more surface cracks are formed during drying on the surface; consequently, the rate of moisture loss is more than the fig. In the case of dates, the rate of moisture reduction during the drying process was very low due to the low initial moisture content (20.03% w.b.).

For all types of products, due to the release of moisture content and viscoelastic stresses in the tissue pores of the samples, the volume of the product decreased by increasing drying time and as a result, volumetric shrinkage increased significantly (Table 1). The results indicated that the most significant change in the amount of volumetric shrinkage occurred in the early drying times in button mushrooms and over time, the amount of these changes decreased. The reason for this is the rapid removal of moisture content from the button mushrooms in the first 4 h of drying (Fig. 3). The highest significant changes in volumetric shrinkage for plums and figs occurred 8 and 10 h after the beginning of drying, respectively (Table 1). This is due to the late formation of cracks in the skin of these fruits, which is accompanied by a further reduction in the internal moisture of the fruit. In the case of dates, the amount of volumetric shrinkage increased slowly over time due to the low rate of moisture reduction during the drying process (Fig. 3 and Table 1). Since the higher coefficient of variation indicates more dispersion of the data compared to their mean value, the dispersion in the volumetric shrinkage rate of date, plum and fig samples was much higher than that for button mushrooms.

Table 1
Mean comparison of volumetric shrinkage values of samples at different drying times.

Drying time (hr)	Sample type Plum	Fig	Date	Mushroom
2	$17.99^{c} \pm 3.69$	$15.99^{e} \pm 1.93$	$4.35^{c} \pm 0.89$	$35.61^{c} \pm 6.84$
4	$22.82^{bc} \pm 8.36$	$22.98^{d} \pm 0.49$	$8.05^{bc} \pm 1.06$	$55.63^{b} \pm 16.94$
6	$30.74^{b} \pm 4.17$	$26.51^{d} \pm 1.03$	$10.90^{ab} \pm 7.54$	$62.95^{ab} \pm 8.59$
8	$45.22^{a} \pm 3.41$	$31.65^{c} \pm 3.10$	$11.88^{ab} \pm 1.16$	$65.71^{ab} \pm 5.03$
10	$46.87^{a} \pm 3.09$	$41.16^{b} \pm 2.01$	$13.69^{ab} \pm 1.54$	$76.84^{a} \pm 2.51$
12	$50.92^{a} \pm 5.16$	$47.17^{a} \pm 3.25$	$14.02^{a} \pm 1.99$	$76.61^{a} \pm 3.89$
Coefficient of variation (%)	37.37	35.62	42.44	25.71

Data have been presented as mean ± standard deviation of volumetric shrinkage values (%) of 5 samples (for the last drying time the number of samples was 7). For each sample type, means followed by the different letters are significantly different (p less than 0.05, one way ANOVA, post-hoc Tukey's HSD test).

Table 2
Accuracy of volume measurement by photogrammetry compared to the fluid displacement method.

Sample type	Size	Volume (cm^3) measured by fluid displacement method	Volume (cm^3) measured by photogrammetry technique	Absolute percentage error (%)
Plum	Small	16.81	16.01	4.76
	Big	23.7	24.92	5.15
Fig	Small	13.65	14.38	5.34
	Big	23.52	23.26	1.11
Date	Small	6.99	6.25	10.58
	Big	11.23	11.96	6.50
Mushroom	Small	8.07	7.84	2.85
	Big	19.62	19.32	1.53

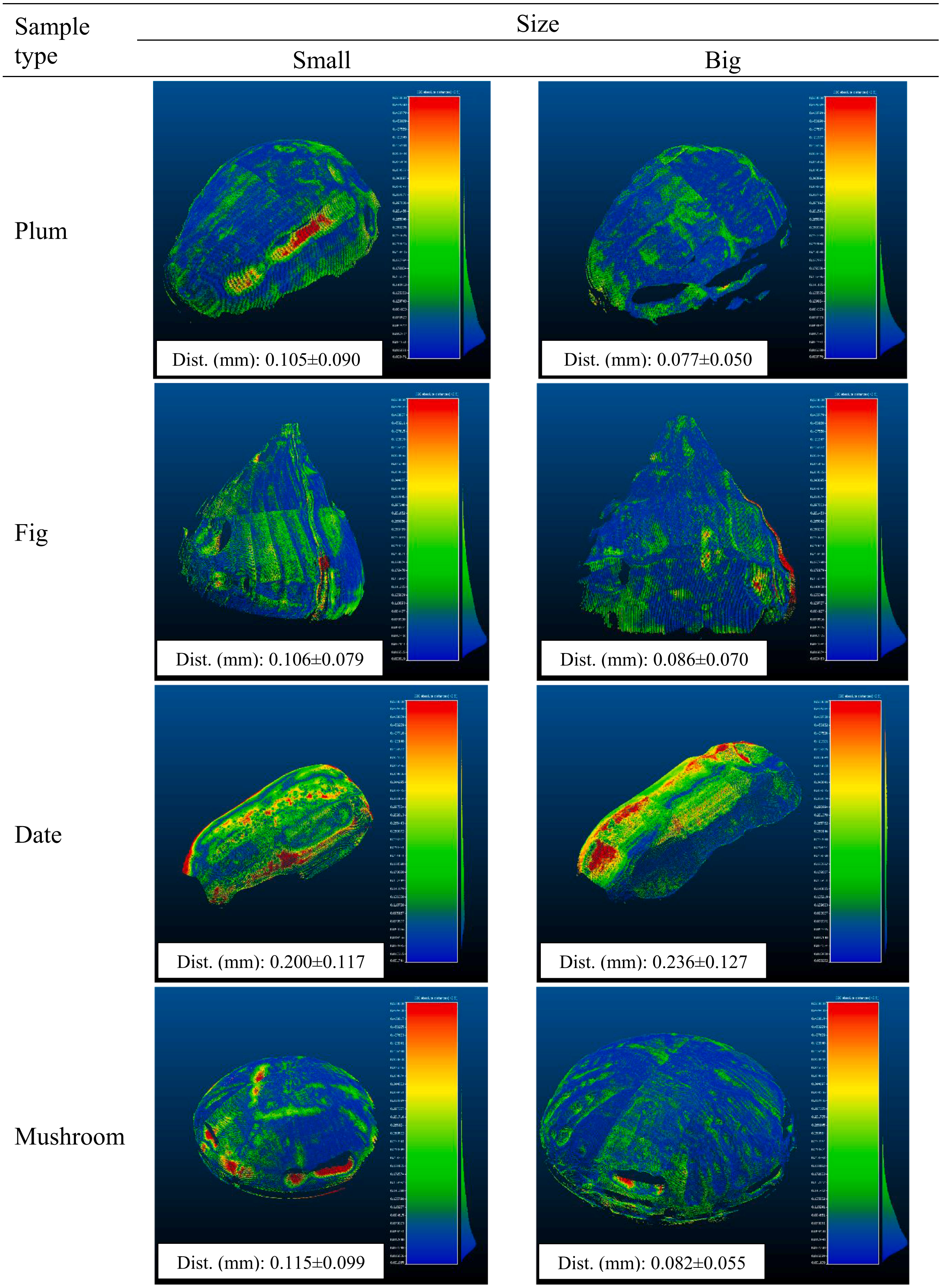

Fig. 4. Heat map of differences between point clouds of 3D laser scanning and photogrammetry of artificial (printed) samples. For each sample type, the point-to-point distance (Dist.) value has been shown as mean ± standard deviation of all points.

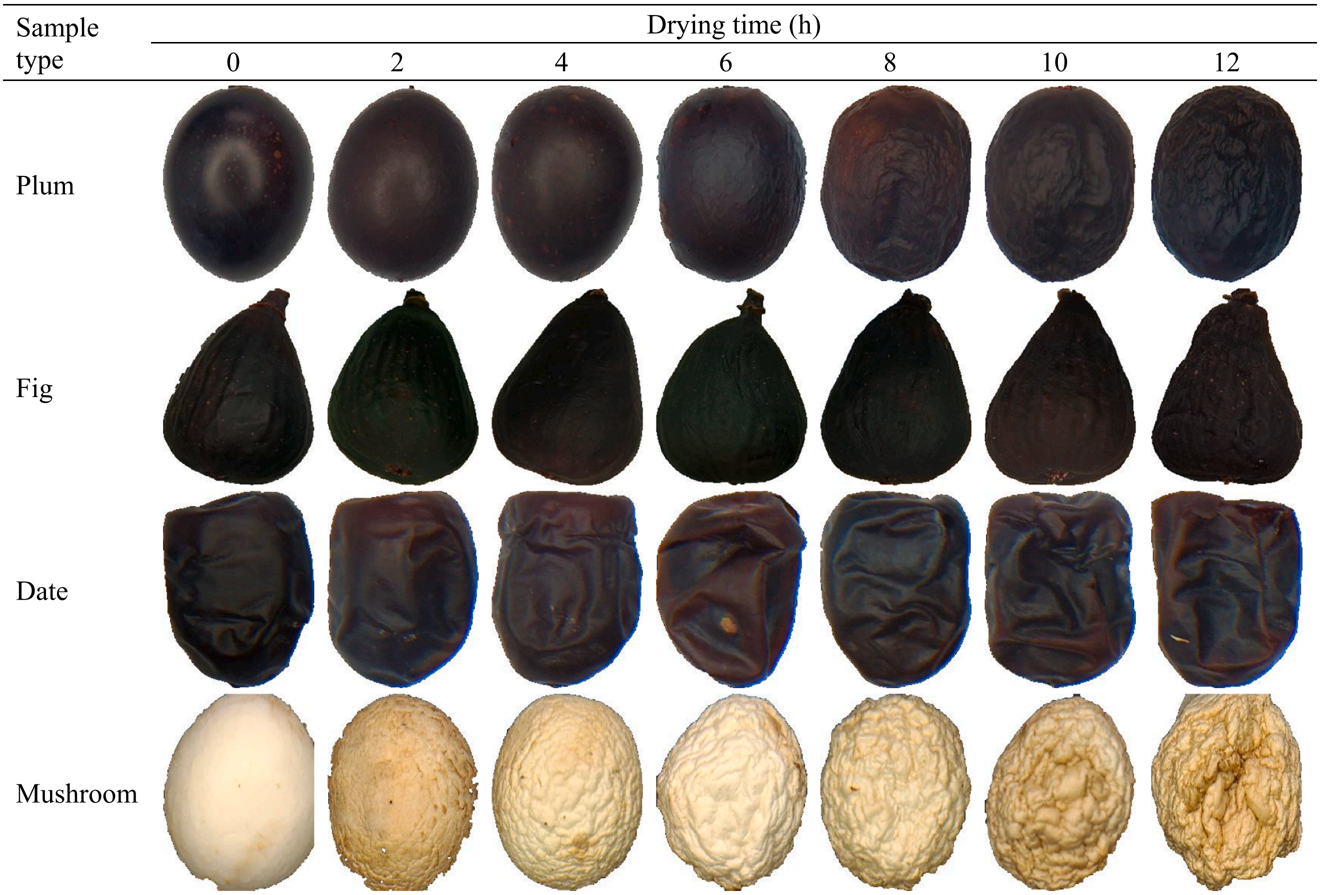

Fig. 5. Example of segmented 2D images of samples during drying process. The non-object (background) pixels have been changed to white for better visualization.

3.2. Geometric validation of the 3D laser imaging system

Table 2 shows the results of the comparison between the photogrammetric volume measurement of artificial (printed) samples and the volume measured with the fluid displacement method. Results show that the volumes determined by the two methods are very close to each other. The mean of the absolute percentage error is only about 4.73 percent. Thus, it is appropriate to apply the 3D reconstruction of the objects by photogrammetry as a reference. Only the data of the date stand out with their almost twice as large deviation. After looking at the image data sets, it can be assumed that the error results from some not perfectly focused images. As a result, some edges and features are not sharply visible in the images. This can result in slight shifts when matching the features, which are responsible for the errors to be detected.

As stated in Section 2.4.3. and 2.5.2., since it was not possible with the laser imaging setup to make a complete 360-degree 3D scan of the objects and only half of them was scanned, the accuracy of the point clouds of the laser scanner cannot be determined by the volume of the objects. Therefore, the point clouds of the laser scanner were registered with the help of an iterative closest point algorithm (ICP) (Besl and McKay, 1992) against the photogrammetrically determined point clouds and then the point-to-point distance was calculated. This results in an error measure that can be used to describe the deviations of the two point clouds. Fig. 4 shows the evaluation for the four different artificial (printed) samples in two sizes each. The coloration from blue to red visualizes the point-to-point deviation, as the heat map, between the photogrammetry and laser scanner data sets. Looking at the figures (mean and standard deviation of the comparison) and the respective histogram for the error distribution, it is noticeable that the errors are almost exclusively in the range less than 0.240 mm. With the exception of the date, the mean error is less than 0.12 mm with a maximum standard deviation of 0.099 mm.

Looking at the model of the plum, it is noticeable that the areas in which larger errors occur are located in valleys of the surface (Fig. 4). These are most likely missing data due to shadowing and this is due to the way the data is recorded. For the photogrammetric 3D reconstruction, the plum was photographed from all directions and from different angles, thus shadowing could be reduced to a minimum. However, since the laser scanner only moves in one plane over the samples, this can cause shadowing in which no data can be recorded. This can also be observed in the two models of figs and mushroom. The larger deviations are also found here in the edges and dimples and are thus mainly due to shading. The only striking thing is the data of the dates. Overall, the mean error of 0.200 mm and 0.236 mm is about twice as large as for all other objects. In addition, the error is very evenly distributed over the entire surface. There are also extreme values in hollows, but overall the error is relatively evenly distributed over the entire surface. Looking back at Table 2, it is noticeable that the photogrammetry dataset of plum and date has an exceptionally high error compared to the other datasets. Thus, it can be assumed that the photogrammetry data set of the plum and date is highly error-prone and the point cloud of the laser scanner is significantly closer to the actual object than it appears.

All in all, the data showed that a volume determination via photogrammetry provides an accuracy comparable to the fluid displacement method. In addition, the surface of a fruit can be measured with high precision and reliability using a 3D laser scanner.

Table 3
Statistical measures of predicting shrinkage of some horticultural products based on the texture features of 2D images.

Sample type	Texture analysis method*	Train R	RMSE (%)	MAPE (%)	Cross-validation R	RMSE (%)	MAPE (%)	Test R	RMSE (%)	MAPE (%)
Plum	FOSH	0.58 ± 0.07	28.62 ± 2.83	58.00 ± 4.89	0.52 ± 0.11	29.03 ± 2.04	57.89 ± 10.21	0.45 ± 0.13	29.77 ± 7.24	68.30 ± 8.38
	GLCM	0.36 ± 0.12	32.29 ± 1.88	68.47 ± 4.51	0.26 ± 0.09	33.30 ± 2.01	70.12 ± 10.67	0.23 ± 0.11	34.30 ± 2.56	73.55 ± 9.04
	GLRLM	0.76 ± 0.05	22.69 ± 2.18	41.61 ± 7.34	0.67 ± 0.09	26.09 ± 3.60	49.11 ± 11.38	0.75 ± 0.05	22.95 ± 2.06	37.68 ± 4.96
	LBP	0.75 ± 0.05	22.95 ± 2.06	37.68 ± 4.96	0.70 ± 0.08	24.82 ± 2.04	41.61 ± 6.37	0.66 ± 0.07	26.09 ± 2.62	41.79 ± 6.34
Fig	FOSH	0.44 ± 0.14	23.29 ± 1.82	51.18 ± 7.30	0.34 ± 0.16	25.15 ± 2.21	53.95 ± 9.32	0.20 ± 0.16	27.58 ± 4.40	60.04 ± 8.15
	GLCM	0.53 ± 0.07	22.38 ± 1.29	47.48 ± 4.84	0.44 ± 0.11	23.52 ± 1.60	50.53 ± 7.69	0.38 ± 0.14	26.99 ± 7.12	54.90 ± 12.49
	GLRLM	0.67 ± 0.06	19.71 ± 1.46	41.51 ± 3.99	0.56 ± 0.09	21.92 ± 1.63	45.34 ± 6.83	0.46 ± 0.10	24.16 ± 3.00	48.66 ± 5.15
	LBP	0.65 ± 0.06	19.93 ± 1.28	39.97 ± 3.23	0.60 ± 0.10	21.05 ± 1.66	43.33 ± 6.61	0.57 ± 0.14	22.78 ± 5.53	47.03 ± 9.73
Date	FOSH	0.39 ± 0.10	4.92 ± 3.70	41.51 ± 3.05	0.27 ± 0.15	5.39 ± 4.03	43.80 ± 7.19	0.28 ± 0.14	5.30 ± 4.09	44.11 ± 5.35
	GLCM	0.38 ± 0.08	4.11 ± 0.23	40.45 ± 3.22	0.32 ± 0.09	4.39 ± 0.56	45.93 ± 8.79	0.20 ± 0.15	4.46 ± 0.52	43.87 ± 8.42
	GLRLM	0.38 ± 0.13	4.14 ± 0.36	42.49 ± 4.88	0.30 ± 0.14	4.17 ± 0.57	42.86 ± 8.11	0.21 ± 0.09	4.45 ± 0.46	43.17 ± 6.98
	LBP	0.31 ± 0.11	4.24 ± 0.21	44.71 ± 2.91	0.24 ± 0.13	4.31 ± 0.37	42.87 ± 7.15	0.12 ± 0.08	4.52 ± 0.38	45.69 ± 5.39
Mushroom	FOSH	0.73 ± 0.06	10.84 ± 1.06	15.22 ± 2.20	0.73 ± 0.09	10.56 ± 1.32	14.22 ± 2.34	0.69 ± 0.09	11.98 ± 1.74	16.56 ± 2.79
	GLCM	0.66 ± 0.03	12.12 ± 0.58	17.53 ± 1.16	0.64 ± 0.09	12.42 ± 1.37	18.23 ± 2.48	0.56 ± 0.09	13.10 ± 1.09	19.01 ± 1.97
	GLRLM	0.76 ± 0.05	10.43 ± 1.20	14.22 ± 2.35	0.69 ± 0.13	11.67 ± 2.51	15.57 ± 3.13	0.66 ± 0.08	12.16 ± 1.60	16.96 ± 2.91
	LBP	0.72 ± 0.05	11.13 ± 0.95	15.84 ± 1.88	0.67 ± 0.08	11.92 ± 1.33	17.18 ± 2.08	0.61 ± 0.09	12.78 ± 1.43	17.61 ± 1.99

* FOSH, GLCM, GLRLM, and LBP stand for 1st order statistics of image histogram, grey level co-occurrence matrix, grey level run length matrix, and local binary pattern, respectively. Data have been presented as mean ± standard deviation of 20 replicates.

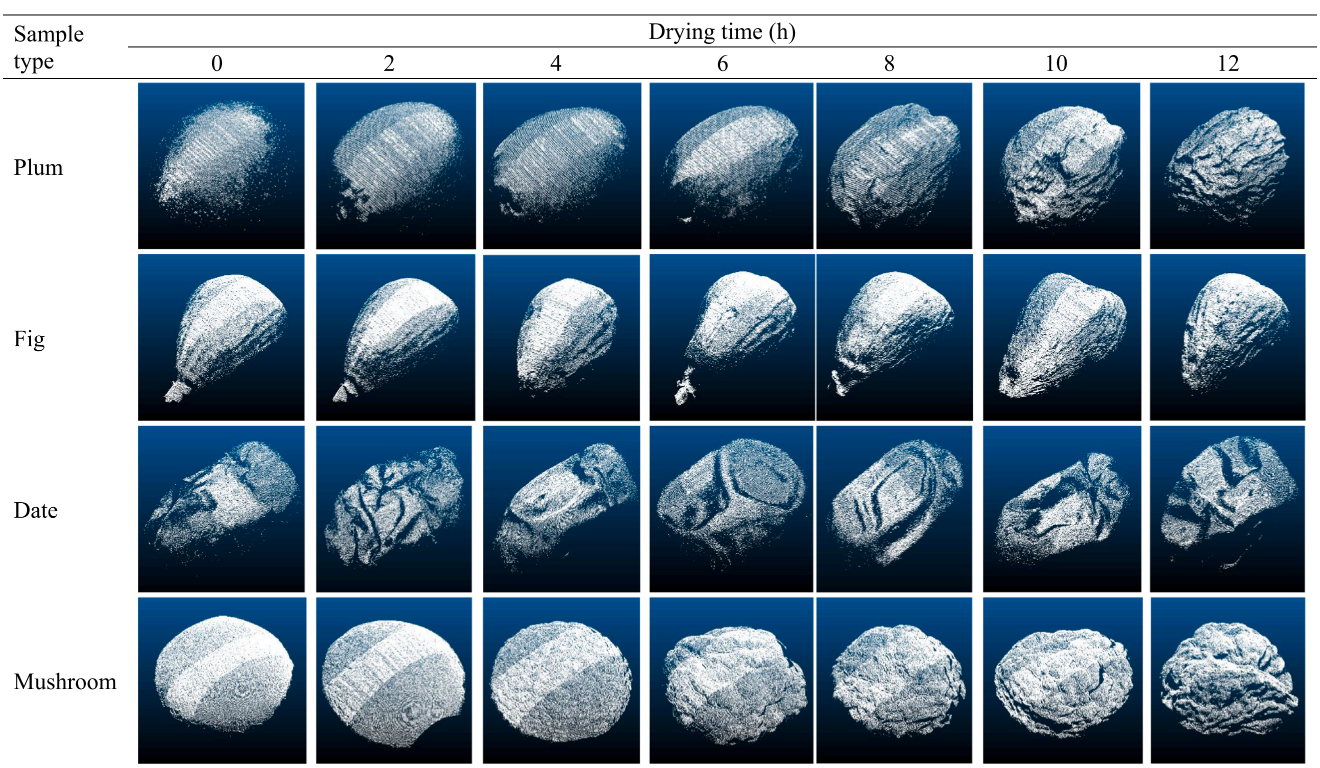

Fig. 6. Examples of point clouds of samples during drying process. The white area at the middle of samples shows the overlap of scans of two consecutive sweeps.

Table 4
Correlation of spatial features extracted from point clouds with volumetric shrinkage.

Spatial feature	Sample type			
	Plum	Fig	Date	Mushroom
PPD_Mean	**−0.747 (0.000)***	−0.061 (0.741)	−0.357 (0.045)	**0.756 (0.000)**
PPA_Mean	**−0.690 (0.000)**	**0.603 (0.000)**	−0.269 (0.136)	**0.423 (0.016)**
SPB_Mean	**0.534 (0.002)**	−0.110 (0.550)	0.281 (0.120)	**−0.635 (0.000)**
PBA_Mean	−0.395 (0.025)	0.270 (0.135)	−0.240 (0.187)	0.375 (0.034)
PPD_Standard deviation	**−0.677 (0.000)**	**−0.562 (0.001)**	−0.372 (0.036)	0.341 (0.056)
PPA_Standard deviation	**−0.813 (0.000)**	−0.006 (0.972)	−0.375 (0.034)	0.060 (0.746)
SPB_Standard deviation	−0.158 (0.378)	**−0.801 (0.000)**	−0.354 (0.047)	**−0.474 (0.006)**
PBA_Standard deviation	−0.388 (0.028)	0.040 (0.829)	−0.302 (0.093)	0.390 (0.027)
PPD_Kurtosis	0.085 (0.645)	**0.414 (0.018)**	0.359 (0.044)	**−0.414 (0.018)**
PPA_Kurtosis	**0.533 (0.002)**	0.290 (0.108)	0.196 (0.282)	0.028 (0.880)
SPB_Kurtosis	0.300 (0.095)	**0.856 (0.000)**	**0.443 (0.011)**	0.234 (0.197)
PBA_Kurtosis	0.028 (0.881)	**0.452 (0.009)**	−0.211 (0.246)	**0.460 (0.008)**
PPD_Skewness	0.159 (0.384)	**−0.418 (0.017)**	0.027 (0.884)	**−0.450 (0.010)**
PPA_Skewness	−0.215 (0.238)	−0.360 (0.043)	−0.124 (0.499)	−0.267 (0.140)
SPB_Skewness	−0.083 (0.653)	**−0.766 (0.000)**	**−0.471 (0.007)**	−0.028 (0.879)
PBA_Skewness	−0.045 (0.805)	0.345 (0.053)	−0.221 (0.223)	**0.436 (0.013)**

* Digits have been shown as the Pearson correlation coefficient (P-Value). PPD, PPA, SPB, and PBA are point to point distance, point to point vectors' angle, slope of the perpendicular bisector vector, and perpendicular bisector vectors' angle, respectively. Selected features have been shown in bold.

3.3. Prediction of volumetric shrinkage based on the texture features of 2D images

Fig. 5 shows that the surface of the products has been wrinkled by increasing the drying time and as a result by reducing the amount of moisture. Button mushroom, plum, and fig showed the highest increase in surface wrinkle over drying time, respectively (Fig. 5). As the moisture content decreases, the cellular tissue of the samples shifts and fills the voids created by exiting moisture from the samples, which leads to a wrinkle on their surface. The amount of wrinkle created on the surface of the products is consistent with changes in their volumetric shrinkage. For plum, from 0 to 6 h and also 8 to 12 h, no significant change is observed in the amount of surface wrinkle (Fig. 5). Changes in volumetric shrinkage were not significant at the above times (Table 1). For fig, surface wrinkle is most evident at 10 and 12 h after the beginning of drying (Fig. 5). Significant changes in volumetric shrinkage at these times also confirm this (Table 1). In the case of button mushroom, as it was occurred for volumetric shrinkage (Table 1), noticeable changes in the surface wrinkle were observed by increasing drying time, so that at 10 and 12 h after the onset of drying, it reached the maximum rate (Fig. 5). Surface wrinkle changes for date at different drying times are not noticeably recognizable (Fig. 5), which is consistent with the absence of significant changes in volumetric shrinkage at 4 to 10 h of drying (Table 1).

Table 3 illustrates the performance of MLP models in predicting volumetric shrinkage of the studied products based on the features extracted from the texture of the images. Overall, the results were not satisfactory for any of the products. The best results were obtained for button mushroom (R_t = 0.69 and $MAPE_t$ = 16.56) in which the MLP model was created using the features derived from the FOSH method. For plum, the MLP model created using the features derived from the GLRLM method had the best performance (R_t = 0.75 and $MAPE_t$ = 37.68). The MLP models created to predict the volumetric shrinkage of fig and date showed very poor performance, so that the best results were obtained using the features derived from the LBP method (R_t = 0.57 and $MAPE_t$ = 47.03) and FOSH method (R_t = 0.28 and $MAPE_t$ = 44.11), respectively. In general, the results indicate that despite the changes in the surface wrinkle of the products during the drying process (as discussed at the beginning of this section), the textural features derived from the 2D images cannot show these changes well. Therefore, the use of textural features derived from 2D images to create volumetric shrinkage predictor models is not recommended.

3.4. Prediction of volumetric shrinkage based on the features of 3D point clouds

Fig. 6 illustrates examples of point clouds obtained for different samples types at different drying times. Visual comparison of the obtained point clouds (Fig. 6) with images from 2D imaging (Fig. 5) shows that laser scanning can illustrate the surface wrinkle better compared to conventional imaging. The matrix of features extracted from point clouds may contain a lot of information that is not necessarily useful for creating a predictive model of volumetric shrinkage, as the use of some of these features may disrupt the prediction process or lead to the presentation of a weak prediction model. In machine learning, the elimination of redundant features and the selection of most informative features have a significant role in learning an efficient model. In this study, a Pearson correlation coefficient based statistical method was used to select superior features from the spatial features matrix extracted from the samples point clouds (Blessie and Karthikeyan, 2012). For each feature vector, the value of its linear correlation to volumetric shrinkage values along with the significance level of the linear relationship was calculated using *t*-test and determining its P-value (Table 4). A higher value of the correlation coefficient (regardless of its sign) indicates a stronger linear relationship between that feature and volumetric shrinkage values. The P-value also indicates the statistical significance of this linear relationship at a certain level of probability. The following criterion was considered to select the superior features:

$$|Pearsoncorrelationcoefficient| \geq 0.400 and P - value \leq 0.050 \tag{11}$$

Table 4 illustrates the correlation coefficient and P-value of the superior features for each of the studied products in bold. Accordingly, the number of features used to create the MLP models for predicting volumetric shrinkage of plum, fig, date, and button mushroom were 6, 8, 2, and 8, respectively. Fig. 7 illustrates the performance of MLP models in predicting the volumetric shrinkage of the studied products based on selected spatial features of point clouds. In general, the performance of MLP models was satisfactory for all products compared to the results obtained using texture analysis of 2D images (Section 3.3). For plum and fig, the percentage of prediction error in the test phase was less than 20% (R = 0.90) and less than 15% (R = 0.95), respectively. The weakest performance of MLP models was related to date in which volumetric shrinkage was predicted with MAPE = 23.54 and R = 0.78. The best results were related to the button mushroom in which the amount of prediction error of volumetric shrinkage in the test stage was less than 10% (R = 0.87). The results indicate that suitable MLP models can be created to predict the volumetric shrinkage of horticultural products during the drying process using spatial features of point clouds.

4. Conclusions

In this study, an approach based on 3D laser imaging was presented to measure the volumetric shrinkage of small-size horticultural products. The results of modeling by multilayer perceptron neural networks and using spatial features extracted from the point clouds obtained from

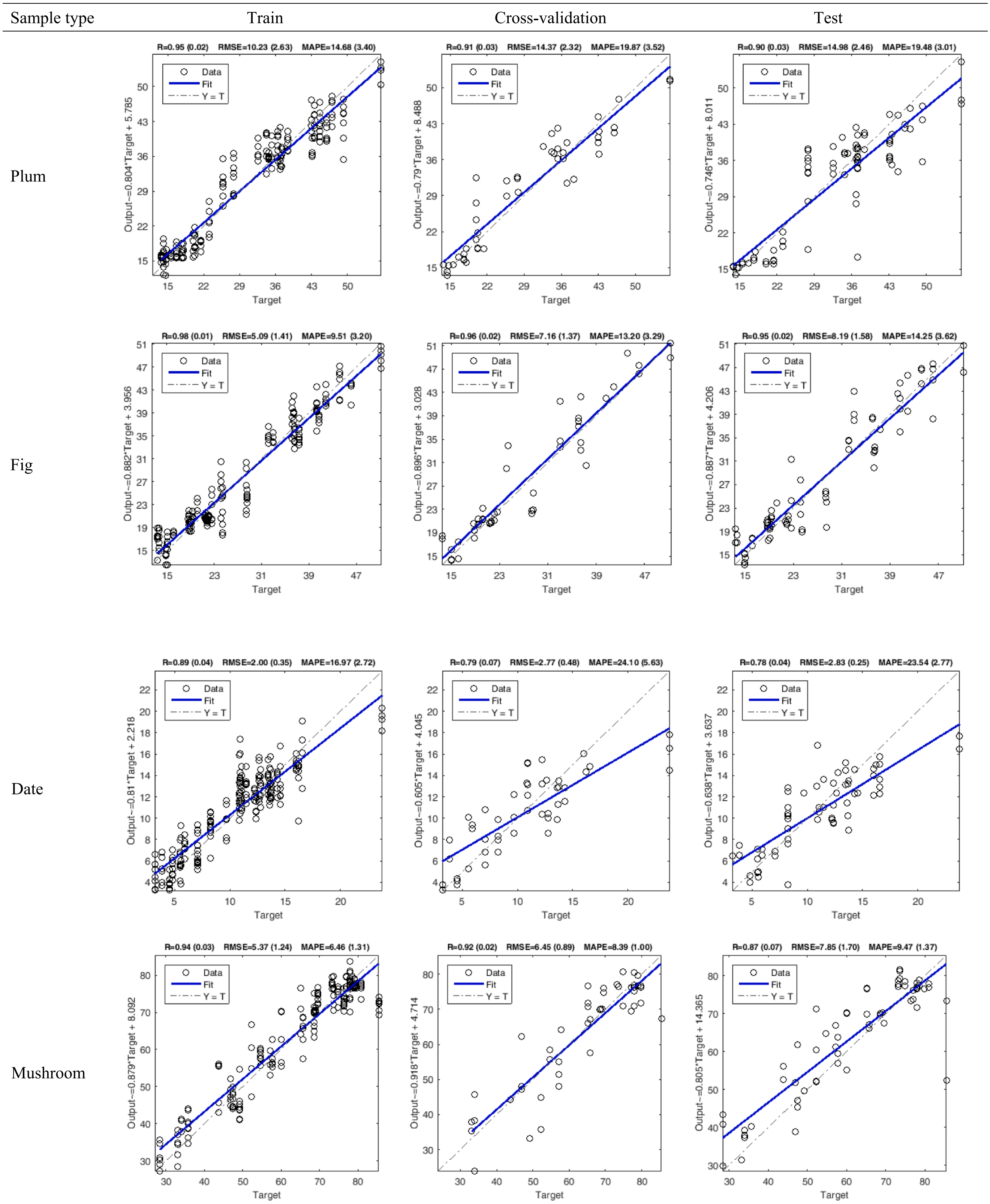

Fig. 7. Statistical measures of predicting volumetric shrinkage of some horticultural products based on the spatial features of point clouds. Data have been presented as mean (standard deviation) of 20 replicates.

scan lines indicate the efficiency of laser imaging method in measuring the volumetric shrinkage of the studied products during the drying process. Since 3D laser imaging requires moving the imaging system or the sample in front of each other to fully scan the surface of the sample, this method is suitable for implementation on moving bed drying machines in which the samples are moving linearly on a conveyor belt inside the dryer chamber. In this case, the dryer can be controlled only using a laser scanner (a linear laser and a digital camera) and using a computer program. Such a system can be implemented at a low cost. Therefore, the immediate results of this research will lead to introducing a new 3D vision approach for real-time scanning the surface of small size horticultural products and measuring volume change during drying process. In this way, volumetric shrinkage could be calculated non-contact as a physical quality characteristic of dry product. Overall, findings of this research would be highly attractive for the food preservation and drying technology industry.

CRediT authorship contribution statement

Kaveh Mollazade: Conceptualization, Supervision, Methodology, Investigation, Data curation, Formal analysis, Resources, Visualization, Writing – original draft. **Joschka van der Lucht:** Methodology, Software, Writing – original draft, Writing – review & editing. **Sven Jörissen:** Software, Writing – review & editing. **Andreas Nüchter:** Supervision, Project administration, Funding acquisition, Writing – review & editing.

Declaration of Competing Interest

The authors declare that they have no known competing financial interests or personal relationships that could have appeared to influence the work reported in this paper.

Data availability

Data will be made available on request.

Acknowledgements

The authors are grateful to the German Research Foundation (DFG-Deutsche Forschungsgemeinschaft) for the financial support through the grant number NU 230/13-1 for project number 445893474. Special thanks goes to Dorit Borrmann and Michael Bleier for their technical advice. Thanks also goes to University of Kurdistan, Iran.

References

Aacc, 1986. Approved methods of the American Association of Cereal Chemists, American Association of Cereal Chemists. Method 66–50. Approved methods of the AACC, 10th ed. St. AACC, Paul, Minn.

Al-Awaadh, A.M., Hassan, B., Ahmed, K.A.M., 2015. Hot air drying characteristics of Sukkari date (*Phoenix dactylifera L.*) and effects of drying condition on fruit color and texture. Int. J. Food Eng. 11 (3), 421–434.

Aprajeeta, J., Gopirajah, R., Anandharamakrishnan, C., 2015. Shrinkage and porosity effects on heat and mass transfer during potato drying. J. Food Eng. 144, 119–128.

Behroozi Khazaei, N., Tavakoli Hashjin, T., Ghassemian, H., Khoshtaghaza, M.H., Banakar, A., 2013. Application of machine vision in modelling of grape drying process. J. Agric. Sci. Technol. 15, 1095–1106.

Besl, P.J., McKay, N.D., 1992. A method for registration of 3-D shapes. IEEE Trans. Pattern Anal. Mach. Intell. 14 (2), 239–256.

Blessie, E.C., Karthikeyan, E., 2012. Sigmis: A feature selection algorithm using correlation based method. J. Algorithms Comput. Technol. 6 (3), 385–394.

Bonazzi, C., Dumoulin, E., 2011. Quality changes in food materials as influenced by drying processes. In: Mujumdar, A.S. (Ed.), Tsotsas E. Wiley-VCH Verlag GmbH, Modern Drying Technology.

Caglarirmak, N., 2011. Physical properties, nutrients and estimated volatiles of Agaricus bisporus (white) at two harvests. Ital. J. Food Sci. 23 (4), 423–430.

Danvind, J., Synnergren, P. 2001. Method for measuring shrinkage behaviour of drying wood using digital speckle photography and X-ray computerised tomography. In: Proceedings of 7th International IUFRO Wood-drying Conference. July 9-13, Tsukuba, Japan. pp 276-281.

Dehghannya, J., Gorbani, R., Ghanbarzadeh, B., 2016. Shrinkage of mirabelle plum during hot air drying as influenced by ultrasound-assisted osmotic dehydration. Int. J. Food Prop. 19, 1093–1103.

Ersoy, N., Gozlekci, S., Gok, V., Yilmaz, S., 2017. Fig (*Ficus carica* L.) fruit: some physical and chemical properties. Acta Hortic. 1173, 329–334.

Girardeau-Montaut, D., 2015. Cloud compare - 3d point cloud and mesh processing software. Open Source Project.

Hiep, V.H., Keriven, R., Labatut, P., Pons, J.P. 2009. Towards high-resolution large-scale multi-view stereo. In: 2009 IEEE Conference on Computer Vision and Pattern Recognition. June 20-25, Miami, FL, USA.

Hirschmuller, H., 2007. Stereo processing by semiglobal matching and mutual information. IEEE Trans. Pattern Anal. Mach. Intell. 30 (2), 328–341.

Ionica, M.E., Nour, V., Trandafir, I., Cosmulescu, S., Botu, M., 2013. Physical and chemical properties of some European plum cultivars (Prunus domestica L.). Not. Bot. Horti. Agrobo. 41 (2), 499–503.

Jafari, A., Bakhshipour, A., 2014. Inspection of quince slice dehydration stages based on extractable image features. Czech J. Food Sci. 32 (5), 456–463.

Jahromi, M.K., Mohtasebi, S.S., Jafari, A., Mirasheh, R., Rafiee, S., 2008. Determination of some physical properties of date fruit (cv. Mazafati), J. Agric. Technol. 4 (2), 1–9.

Lewicki, P.P., Jakubczyk, E., 2004. Effect of hot air temperature on mechanical properties of dried apples. J. Food Eng. 64 (3), 307–314.

Li, J., Bennamoun, L., Fraikin, L., Salmon, T., Toye, D., Schreinemachers, R., Leonard, A., 2014. Analysis of shrinkage effect on mass transfer during convective drying of sawdust/sludge mixtures. Dry. Technol. 32, 1706–1717.

Li, X., Liu, Y., Gao, Z., Xie, Y., Wang, H., 2021. Computer vision online measurement of shiitake mushroom (*Lentinus edodes*) surface wrinkling and shrinkage during hot air drying with humidity control. J. Food Eng. 292, 110253.

Madiouli, J., Sghaier, J., Orteu, J.J., Robert, L., Lecomte, D., Sammouda, H., 2011. Non-contact measurement of the shrinkage and calculation of porosity during the drying of banana. Dry. Technol. 29, 1358–1364.

Mayor, L., Sereno, A.M., 2004. Modelling shrinkage during convective drying of food materials: A review. J. Food Eng. 61, 373–386.

Mollazade, K., Arefi, A., 2017. *LightScatter:* A comprehensive software package for non-destructive monitoring of horti-food products by monochromatic imaging-based spatially-resolved light scattering technology. Comput. Electron. Agric. 142 (B), 597–606.

Mollazade, K., Jörissen, S., Nüchter, A., 2021. Measuring internal quality traits in egg by 3D laser imaging. J. Food Eng. 291, 110289.

Mujumdar, A.S., 2004. Research and development in drying: Recent trends and future prospects. Dry. Technol. 22 (1–2), 1–26.

Nindo, C.I., Sun, T., Wang, S.W., Tang, J., Powers, J.R., 2003. Evaluation of drying technologies for retention of physical quality and antioxidants in asparagus (Asparagus officinalis, L.). LWT - Food Sci. Technol. 36, 507–516.

Poliarnyi, N. 2021. Out-of-core surface reconstruction via global TGV minimization. In: Proceedings of the IEEE/CVF International Conference on Computer Vision. October 11-17, Montreal, BC, Canada.

Raponi, F., Moscetti, R., Monarca, D., Colantoni, A., Massantini, R., 2017. Monitoring and optimization of the process of drying fruits and vegetables using computer vision: a review. Sustainability. 9 (11), 1–27. https://doi.org/10.3390/su9112009.

Sacilik, K., Elicin, A.K., Unal, G., 2006. Drying kinetics of Uryani plum in a convective hot-air dryer. J. Food Eng. 76, 362–368.

Sarvestani, F.S., Rahimi, A., Hatamipour, M.S., 2014. An experimental study on drying characteristics and kinetics of figs (*Ficus carica*). Pol. J. Chem. Technol. 16 (4), 60–65.

Schöning, J., Heidemann, G. 2015. Evaluation of multi-view 3D reconstruction software. In: International conference on computer analysis of images and patterns. September 2-4, Valletta, Malta. pp 450-461.

Vaskoska, R., Ha, M., Tran, H.T.T., Khoshelham, K., White, J.D., Warner, R.D., 2020. Evaluation of 3D laser scanning for estimation of heating-induced volume shrinkage and prediction of cooking loss of pork cuboids compared to manual measurements. Food Bioproc. Tech. 13 (6), 938–947.

Yadollahinia, A., Jahangiri, M., 2009. Shrinkage of potato slice during drying. J. Food Eng. 94, 52–58.

Yan, Z., Sousa-Gallagher, M.J., Oliveira, F.A.R., 2008. Shrinkage and porosity of banana, pineapple and mango slices during air-drying. J. Food Eng. 84, 430–440.